ACS Catalysis

pubs.acs.org/acscatalysis Research Article

Cyano Substituent on the Olefin Linkage: Promoting Rather than Inhibiting the Performance of Covalent Organic Frameworks

Yongliang Yang, Na Luo, Shiyun Lin, Huan Yao, and Yaqi Cai*

Cite This: ACS Catal. 2022, 12, 10718−10726 Read Online

ACCESS | Metrics & More | Article Recommendations | Supporting Information

ABSTRACT: It is generally believed that the electron-withdrawing cyano group in the olefin linkage would inhibit the stability and π-conjugation of covalent organic frameworks (COFs), which raises concerns about their optoelectronic properties. However, the structure−activity relationship between the structure of olefin linkages and properties of COFs is still inconclusive. In this work, imine-, vinylene-, and acrylonitrile-linked COFs with identical triphenyltriazine building blocks were designed and synthesized. Our work demonstrated that construction of acrylonitrile linkages not only enhanced the chemical stability and photostability but also led to remarkable optoelectronic properties with a record fluorescence quantum yield of 35.37% in the solid state. Further, the acrylonitrile linkage endows TTAN-COF/Pt NPs with superior and durable photocatalytic activity in both the hydrogen evolution reaction (11.94 mmol g^{-1} h^{-1}; BET surface area, 739.28 m^2 g^{-1}) and aerobic oxidation reaction. This work demonstrates that the acrylonitrile linkage can significantly enhance the optoelectronic properties and photocatalytic activities of COFs compared with the highly π-conjugated vinylene linkage, providing a valuable reference for the design of optoelectronic functional materials.

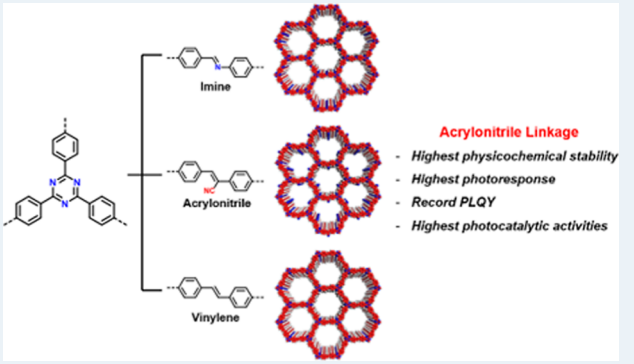

KEYWORDS: *covalent organic frameworks, olefin linkage, heterogeneous photocatalysis, hydrogen evolution, photoluminescence*

INTRODUCTION

As a kind of crystalline and porous organic polymer, covalent organic frameworks (COFs) have attracted great interest of researchers since they were first reported by Yaghi's group in 2005.[1] A variety of COFs have been designed and applied in the fields of separation,[2−5] catalysis,[6−9] energy,[10−13] photovoltaics,[14−17] biomedicine,[18] sensors,[19] environment,[20] and so forth due to the broad artificial design and assembly space of COFs provided by the adjustability of organic building blocks and linkages.[21−23] It is worth noting that photocatalysis has become an important application area of COFs,[24,25] which is due to several characteristics of COFs: (i) extended π-conjugated frameworks, endowing the COFs with the properties of an opto-semiconductor and providing effective conduction paths for carriers; (ii) structural adjustability, implying that the chemical structure can be easily adjusted artificially to fine-tune the band structure of the material; and (iii) large surface areas, providing more accessible reactive sites and reducing the distance of carrier conduction to the reaction interface, thus restraining the electron−hole recombination. After the first report by Lotsch's group,[26] COF photocatalysts have been widely developed in the fields of photocatalytic organic reaction,[27−29] contaminant degradation,[30,31] water splitting,[32−34] and CO_2 reduction.[35,36]

As the key component, the linkage unit greatly determines the properties of COFs, especially the stability. In the context of insufficient chemical stability of conventional borate esters and imine linkages, the development of robust linkages is essential to promote the practical applications of COFs. At the same time, the novel linkage endowed COFs with additional features, for example, a variety of olefin-linked COFs have been reported with promising applications in the field of photocatalysis due to the efficient π-electron delocalization of the olefin linkage.[37] To date, the vinylene (−CH═CH−) linkage and the acrylonitrile [−CH═C(CN)−] linkage are the two main kinds of olefin linkage of COFs. Although it is widely believed that the chemical stability and π-electron delocalization of the olefin linkage would be weakened by the electron-withdrawing cyano substituents, the impact of these two linkages on the stability and photocatalytic activity of COFs is still undefined. Because the construction of vinylene-linked COFs currently relied on several specially designed mono-

Received: June 15, 2022
Revised: July 31, 2022
Published: August 17, 2022

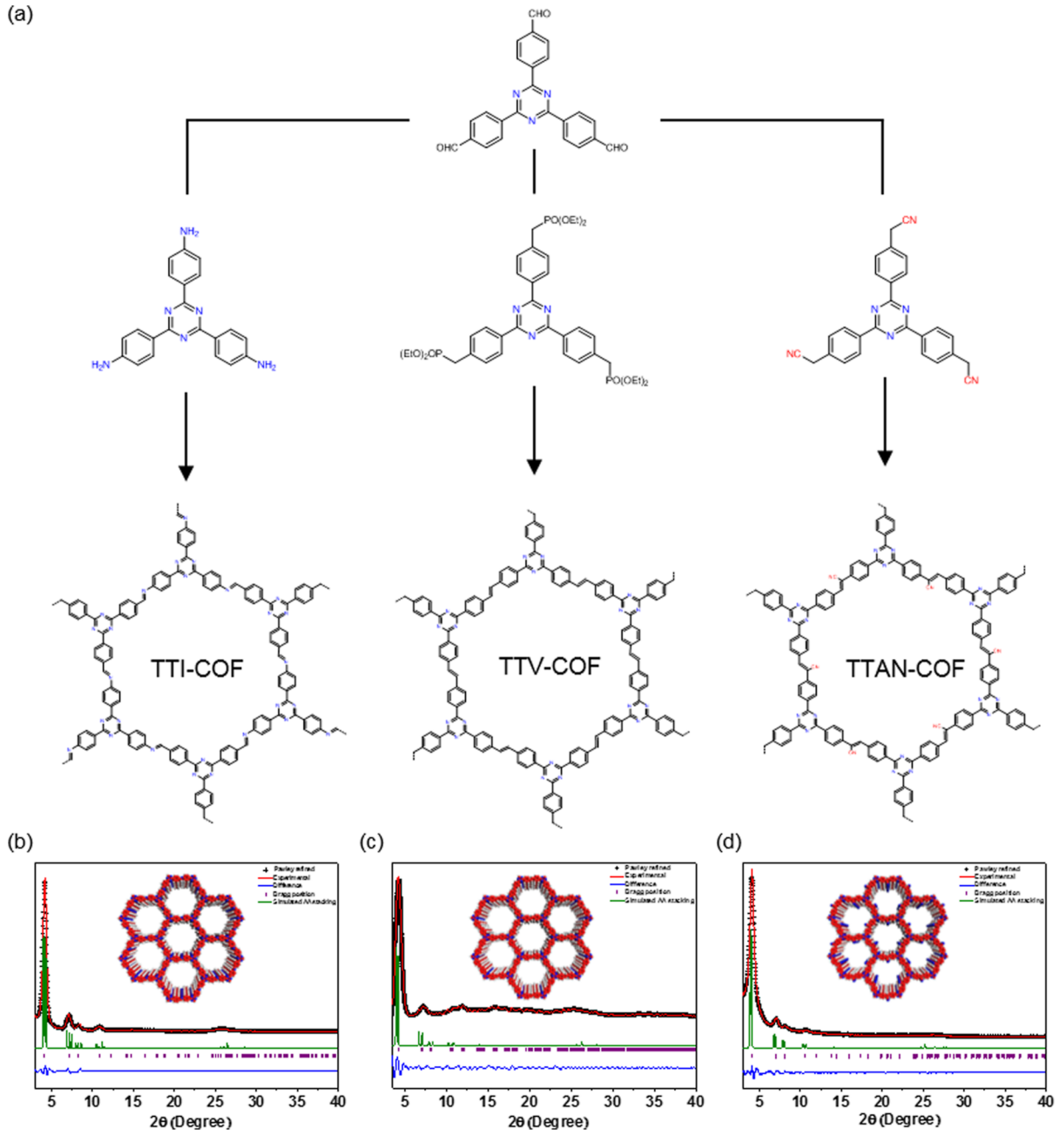

Figure 1. Synthesis and PXRD patterns of TTI/TTV/TTAN-COFs. (a) Illustration of synthetic procedures for three COFs. PXRD patterns for TTI-COF (b), TTV-COF (c), and TTAN-COF (d): comparison between the experimental (red) and Pawley refined (black) profiles, the simulated patterns for the eclipsed AA stacking mode (green), the Bragg positions (purple), and the refinement differences (blue). Insets: the crystal structures of corresponding COFs are viewed along the (001) direction.

mers,[38−43] it is difficult to synthesize vinylene- and acrylonitrile-linked COF materials with identical organic building blocks. After the successful synthesis of vinylene-linked COFs via the Horner−Wadsworth−Emmons (HWE) reaction reported by Feng's group,[44] the chemical structure of vinylene-linked COFs was no longer restricted. It is possible to investigate and compare the effects of two olefin linkages and conventional imine linkages on the properties of COFs.

Herein, three COFs with imine, vinylene, and acrylonitrile linkages with the identical 2,4,6-triphenyl-1,3,5-triazine (N_3) building block were constructed, and the relationship between the linkage structure, stability, and physicochemical properties was further investigated in detail. Our studies revealed the significant advantages of acrylonitrile linkage over imine and vinylene linkages, which greatly enhance the stability and optoelectronic properties of COFs with the record fluorescence quantum yield. Furthermore, the acrylonitrile-linked TTAN-COF showed superior photocatalytic activity to the other two COFs in both hydrogen evolution (in the presence of a Pt co-catalyst) and aerobic oxidation reactions. These results not only break the general opinion that a non-substituent vinylene linkage would endow COFs with better properties but also provide a way to modulate the performance of COFs from the linkage structure.

https://doi.org/10.1021/acscatal.2c02908
ACS Catal. 2022, 12, 10718−10726

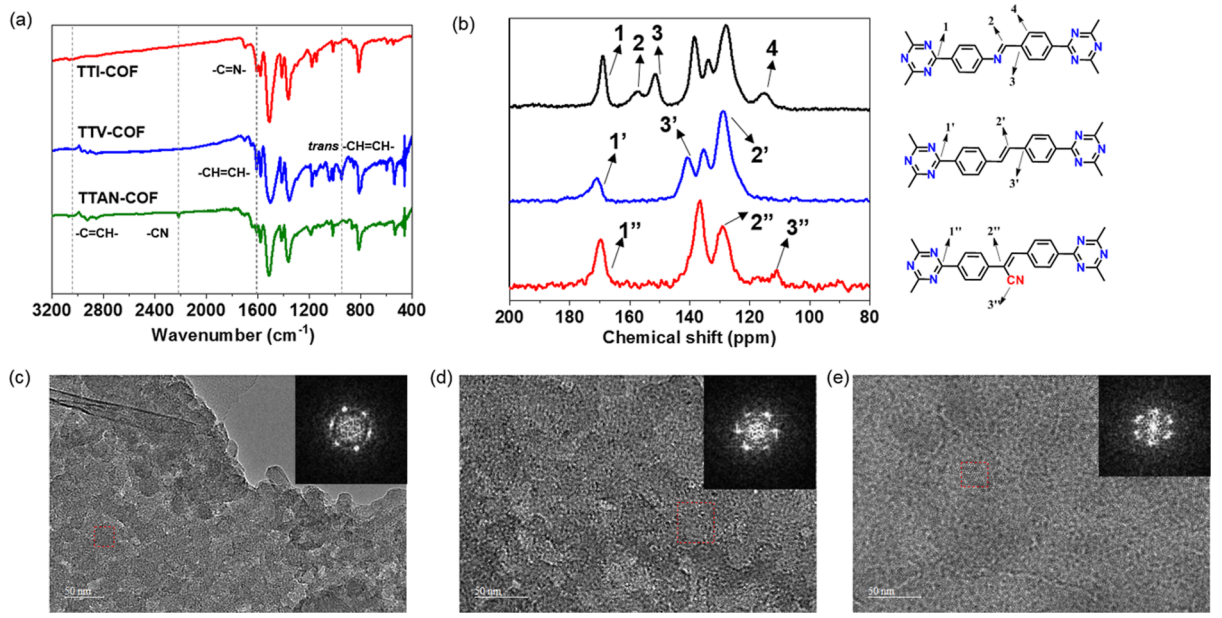

Figure 2. Characterization of TTI/TTV/TTAN-COFs. (a) FT-IR spectra, (b) ^{13}C CP/MAS NMR spectra, and (c−e) TEM images of TTI-COF (c), TTV-COF (d), and TTAN-COF (e). Inset: FFT patterns of the red dotted area in TEM images.

RESULTS AND DISCUSSION

Synthesis and Characterization. COFs with 2,4,6-triphenyl-1,3,5-triazine (N_3) building blocks generally showed high crystallinity and photocatalytic activity due to the high planarity of the N_3 structure[33] and the photoactivity of the triazine unit. Hereby, four monomers with the N_3 structure, 2,4,6-tris(4-formylphenyl)-1,3,5-triazine (TFPT), 2,4,6-tris(4-aminophenyl)-1,3,5-triazine (TAPT), 2,4,6-tris[4-(diethylphosphonomethyl)phenyl]-1,3,5-triazine (TDPT), and 2,4,6-tris(4-cyanomethylphenyl)-1,3,5-triazine (TCPT) were designed and synthesized. As shown in Figure 1, imine-linked TTI-COF was synthesized through the Schiff-base condensation of TFPT and TAPT, vinylene-linked TTV-COF was synthesized through the HWE reaction between TFPT and TDPT, and acrylonitrile-linked TTAN-COF was synthesized through the Knoevenagel condensation of TFPT and TCPT, respectively.

The crystallinity structures of these three COFs were confirmed by the powder X-ray diffraction (PXRD) analysis (Figure 1b−d). The PXRD patterns showed diffraction peaks at 2θ = 4.18, 7.05, 8.48, 10.81, and 25.76° for TTI-COF, 2θ = 4.20, 7.16, 8.30, 11.23, and 25.37° for TTV-COF and 2θ = 4.08, 7.09, 8.05, 10.56, and 25.90° for TTAN-COF, originating from (100), (110), (200), (210), and (001) planes, respectively. The structure models of three COFs were simulated in the hexagonal structure with hcb topology. The experimental PXRD patterns of the three COFs are more likely to match the simulated diffraction patterns of the AA-stacking models (Figure S2). After Pawley refinement of experimental PXRD patterns, the diffraction patterns were in good agreements with the hexagonal unit cells of TTI-COF (P1, a = 26.12 Å, b = 25.74 Å, c = 3.71 Å, α = 87.03°, β = 70.39°, γ = 120.08°, R_p = 5.73%, and R_{wp} = 4.58%), TTV-COF (P1, a = 26.30 Å, b = 26.42 Å, c = 3.65 Å, α = 107.82°, β = 70.59°, γ = 119.79°, R_p = 3.41%, and R_{wp} = 2.15%), and TTAN-COF (P1, a = 26.38 Å, b = 26.30 Å, c = 3.66 Å, α = 78.54°, β = 87.52°, γ = 120.70°, R_p = 5.38%, and R_{wp} = 3.96%).

The chemical structures of the three COFs were analyzed by Fourier transform infrared (FT-IR) and solid-state ^{13}C cross-polarization magic angle spinning (CP/MAS) NMR spectroscopy (Figure 2a,b). In the FT-IR spectrum of TTI-COF, the characteristic peaks at 1625 cm^{-1} corresponding to the C═N bond confirmed the formation of imine linkage. The C═C stretching peaks at 1625 cm^{-1} and the trans −HC═CH− stretching peaks at 970 cm^{-1} in the spectrum of TTV-COF indicated the presence of vinylene linkage with a *trans*-configuration. The acrylonitrile structure of TTAN-COF was demonstrated by the existence of C═C−H and C≡N stretching bands at around 3030 and 2214 cm^{-1}, respectively. All of the ^{13}C NMR spectra of the three COFs exhibited the signals at ∼170 ppm assigned to triazine carbons. The signal at ∼158 ppm of TTI-COF corresponding to imine carbon confirmed the formation of imine linkage. The strong peaks at ∼128 ppm of TTV-COF and TTAN-COF originate from the aromatic carbons and olefinic linkage carbons. Additionally, the signal at ∼112 ppm of TTAN-COF indicated the existence of cyano groups in acrylonitrile linkage. All these results essentially verify the structural integrity of the three COFs.

The permanent porosities of COFs were assessed by measuring nitrogen adsorption isotherms at 77 K (Figure S3). In their nitrogen sorption isotherms, all these COFs feature a type-I reversible isotherm, suggesting their microporous structure. The Brunauer−Emmett−Teller (BET) surface areas of the TTI-COF, TTV-COF, and TTAN-COF were calculated to be 1659.48, 532.82, and 739.28 $m^2\ g^{-1}$, with total pore volumes of 0.702, 0.301, and 0.396 $cm^3\ g^{-1}$, respectively. However, the theoretical specific surface areas of TTI/TTV/TTAN-COF are similar due to their similar structure, calculated to be 2466, 2129, and 2381 $m^2\ g^{-1}$. In fact, the crystallinity and porosity of COF products are greatly affected by the reversibility of the condensation reaction. The condensation reaction with high reversibility is beneficial to the synthesis of COF products with high crystallinity and porosity. In this work, the Schiff base reaction is the most reversible, and the HWE reaction is the least reversible among the three COF

https://doi.org/10.1021/acscatal.2c02908
ACS Catal. 2022, 12, 10718−10726

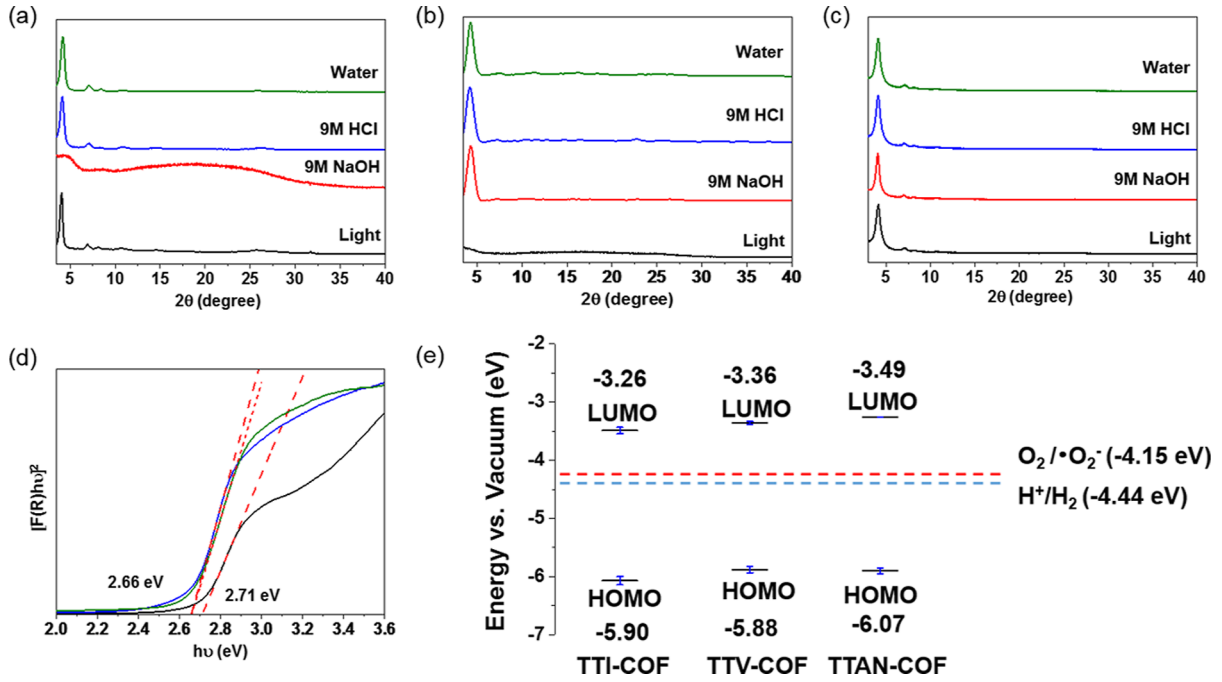

Figure 3. Stability and band alignment of TTI/TTV/TTAN-COFs. PXRD patterns of TTI-COF (a), TTV-COF (b), and TTAN-COF (c) after 1 day treatment in water, 9 M HCl, 9 M NaOH, and visible light (λ > 400 nm) irradiation. Tauc plots (d) and band alignment (e) of TTI/TTV/TTAN-COFs. Error bars denate standard deviation.

synthesis reactions, resulting in obvious differences in the porosity of the three COFs. Furthermore, the pore size distributions (PSDs) of COFs were evaluated using the quenched solid density functional theory (QSDFT) by applying the cylindrical pore model, deriving the dominant distribution at 1.92, 1.88, and 1.95 nm for TTI-COF, TTV-COF, and TTAN-COF, respectively, which are in line with their AA eclipsed model.

Scanning electron microscopy (SEM) images of three COFs (Figure S4) depict the rod-like morphology, due to the high planarity of the N_3 structure, which facilitates the accumulation of COFs along the *Z*-axis during the growth process.[45] The high-resolution transmission electron microscopy (HR-TEM) images of all the three COFs revealed the distinct honeycomb-like internal structures (Figure 2c−e). Meanwhile, the (100) lattice plane with an interplanar spacing of ca. 2.0 nm can be observed, which are in accord with the PSD results and the diffraction peak of the 100 plane in PXRD patterns.

Stability Test. The chemical stability and photo-stability of the three COFs have been investigated (Figure 3a−c). Both TTV-COF and TTAN-COF with the irreversible vinylene and acrylonitrile linkages retained high crystallinity after soaking them in strong acid (9 M HCl), strong alkaline (9 M NaOH), and neutral (water) conditions for 1 day. In contrast, due to the reversibility of imine linkage, structural collapse of TTI-COF was observed after soaking in strong alkaline conditions (9 M NaOH) for 1 day. The above results indicated that the irreversible C═C linkages endowed COFs with superior chemical stability. Although the strong electron-drawing cyano group could make the C═C linkage reversible,[46] our results and previous reports[47] confirmed that the chemical stability of acrylonitrile-linked COFs was high enough to withstand extreme conditions. Additionally, after illumination under a 300 W Xe lamp with a λ > 400 nm cutoff filter in the CH_3CN suspension for 1 day, the PXRD patterns of TTI-COF and TTAN-COF showed negligible change. However, the crystalline structure of TTV-COF was collapsed after illumination, which should be attributed to the [2 + 2] photocycloaddition[48,49] of the vinylene linkages given the distance of ca. 3.6 Å between the two C═C bonds along the parallel orientation in the AA stacking model. In contrast, the π-conjugation of C=C bond in acrylonitrile linkage was weakened by the electron-withdrawing cyano substituent, which hindered the photocycloaddition and significantly improved the photo-stability of acrylonitrile-linked TTAN-COF. The above results suggested that acrylonitrile-linked TTAN-COF possessed both good chemical and photo-stability among the three COFs.

Optical and Electronic Properties. The ultraviolet/visible diffuse reflectance spectra (UV/vis DRS) (Figure S5) revealed the broad absorption band of all the three COFs from 200 to 500 nm. TTI-COF showed an absorption edge at ca. 410 nm, while the TTV-COF showed obviously red-shifted absorption edges at ca. 430 nm. The observed red shift is mainly attributed to the more efficient π-conjugation transmission of the vinylene linkage. A slightly blue-shifted absorption edge at ca. 425 nm compared to TTV-COF was found for TTAN-COF due to the weak π-electron delocalization. Furthermore, the optical band gaps of three COFs were derived from the Tauc plot (Figure 3d). TTV-COF and TTAN-COF possessed a similar optical band gap (2.66 eV), which are narrower than TTI-COF (2.71 eV). To further determine the highest occupied molecular orbital (HOMO) and the lowest unoccupied molecular orbital (LUMO) levels, the cyclic voltammetry (CV) curves of three COFs were measured (Figures S6, S7, Table S4). As shown in Figure 3e, the LUMO levels of three COFs were more negative to both of the redox potential E ($O_2/O_2^{\bullet-}$) and E (H^+/H_2), indicating that the visible light-driven reactions of both H_2 evolution from water splitting and generation of superoxide radicals from oxygen molecule excitation are thermodynami-

https://doi.org/10.1021/acscatal.2c02908
ACS Catal. 2022, 12, 10718−10726

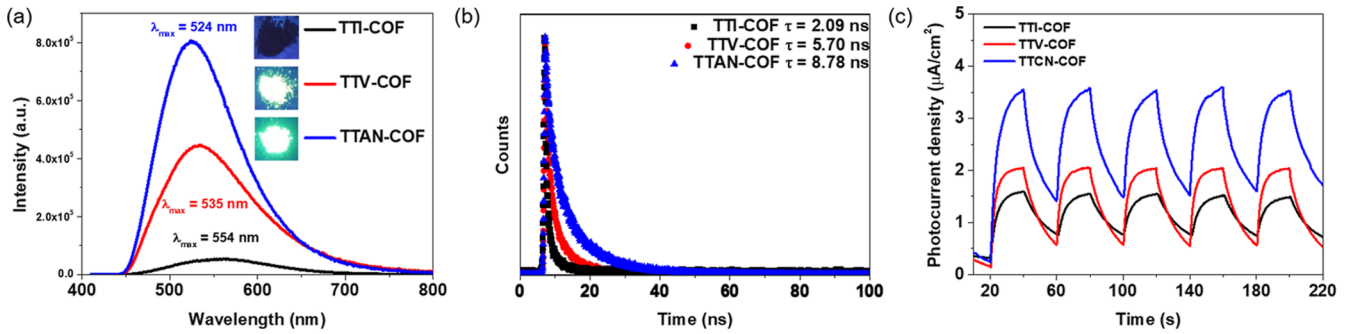

Figure 4. Photoelectric characterization of TTI/TTV/TTAN-COFs. (a) PL spectra, (b) time-resolved fluorescence decay curves, and (c) photocurrent test.

cally feasible. It should be noted that the energy levels obtained by the CV test were used to preliminarily screen the materials that were able to undergo the corresponding reaction. Considering that there are always certain overpotentials in the hydrogen evolution reaction pathways, the actual reaction characteristics of the materials still need to be further explored through experiments. Mott−Schottky plot indicated that all the three COFs are n-type semiconductors due to the positive slope, and the flat band potential were derived as −1.21, −1.14, and −0.98 V vs normal hydrogen electrode (NHE) (Figure S8, Table S5). According to previous reports, the flat band potential of n-type semiconductors is generally more positive than their corresponding LUMO levels.[50] Additionally, we carried out density functional theory (DFT) calculations to further understand the energy band structure of COFs (Figure S10). The theoretically calculated results of energy levels and band gaps showed similar trends to the experimental results. The partial density of states (PDOS) of three COFs were analyzed, manifesting that the HOMO and LUMO of the three COFs were all mainly contributed by the 2p orbital of C atoms. These results indicated that the semiconductor optical properties of the three COFs mainly originated from the extended π-delocalization framework.

Olefin-linked TTV/TTAN-COF solid powders were observed to emit a strong green fluorescence under UV light irradiation, while TTI-COF produced weak yellow fluorescence (Figure 4a). Furthermore, photoluminescence (PL) and time-resolved fluorescence decay analyses were conducted to give an insight into photo-generated electronic behavior of COFs. PL spectra showed that the fluorescence intensity of TTAN-COF is about twice that of TTV-COF. The $\pi-\pi$ interaction between planarized π-conjugated units was generally unfavorable for fluorescence emission, which is known as the phenomenon of aggregation-caused quenching (ACQ).[51] However, the cyano-substituted stilbene linkage unit proved to be an aggregation-induced emission (AIE) reactive group[52] because the bulky and polar CN group in the acrylonitrile linkage is able to confine the $\pi-\pi$ interaction between the parallel cyanostilbene unit in the 2D COF plane, thus resulting in the formation of J-aggregation state[53] that greatly enhances the fluorescence of TTAN-COF. In addition, TTAN-COF exhibited a blue shift of 11 nm in the maximum emission wavelength relative to TTV-COF due to the weakened π-conjugation of 2D COF plane by cyano groups. The weak fluorescence of TTI-COF was attributed to the reduced π-conjugation of the imine linkage and the non-radiative relaxation caused by the internal rotation of the imine bond.[54] The photoluminescence quantum yields (PLQYs) of TTI/TTV/TTAN-COF in the solid state were determined to be 0.79, 6.08, and 35.37%, respectively. Notably, the 35.37% PLQY of TTAN-COF is the highest level among the reported COF materials so far (Table S6). We anticipated that the PLQY of acrylonitrile-linked COF materials can be further significantly improved by further introducing efficient AIE chromophores. Many reports suggested that materials with stronger fluorescence generally exhibited poorer photocatalytic activities due to the fact that the processes of fluorescence and photocatalysis are associated with different types of photo-generated carriers.[55] However, if the catalytic active sites are located on the fluorescent chromophore to share the same type of photo-generated carriers, the fluorescence effect of materials would be positively correlated with the photocatalytic activities. Moreover, TTAN-COF showed the longest transient fluorescence lifetime (8.78 ns) compared to TTI-COF (2.09 ns) and TTV-COF (5.70 ns) (Figure 4b), implying more efficient electron transfer and lower recombination rate of photogenerated carriers in the TTAN-COF. The strongest photocurrent intensity was observed in the TTAN-COF photoelectrode among the three COFs (Figure 4c), indicating best photo−electric activity and more efficient transfer of photo-induced carriers in acrylonitrile-linked COFs. The above experimental results indicated that the electron-withdrawing-CN substituent appended to the olefin linkage significantly promotes the photoelectric properties of COF materials. Good photocatalytic activities are also anticipated.

Photocatalytic H_2 Evolution Reaction. First, the photocatalytic H_2 evolution performance of the three COFs was evaluated. 10 mg of photocatalyst was dispersed in 50 mL deionized water with visible light (λ > 420 nm) irradiation at 8 °C. A 3 wt % platinum co-catalyst was in situ photo-deposited on the COFs. When 10 vol % of triethanolamine (TEoA) (pH 10.30) was chosen as a sacrificial electron donor (SED), the trend of average H_2 evolution reaction (HER) rates was TTI-COF < TTV-COF < TTAN-COF (BET surface area: 1659.48, 532.82 and 739.28 $m^2 \cdot g^{-1}$), which were determined to be 1.21, 116.58, and 698.68 μmol g^{-1} h^{-1}, respectively (Figure S11). It is noted that some imine COFs with similar structure also exhibited poor activity of photocatalytic H_2 evolution reaction with TEoA as the SED, which was attributed to the high oxidation potential of TEoA.[56] In contrast, ascorbic acid (AC) was generally a good SED for photocatalytic H_2 evolution reactions (HERs) of imine COFs due to the protonation of imines under acidic conditions. When 0.1 M AC was applied as SED, TTI-COF, TTV-COF, and TTAN-COF exhibited significantly enhanced HER rates of 0.46, 5.50, and 11.94 mmol g^{-1} h^{-1} (Figure 5a). Notably, the HER activity of

https://doi.org/10.1021/acscatal.2c02908
ACS Catal. 2022, 12, 10718−10726

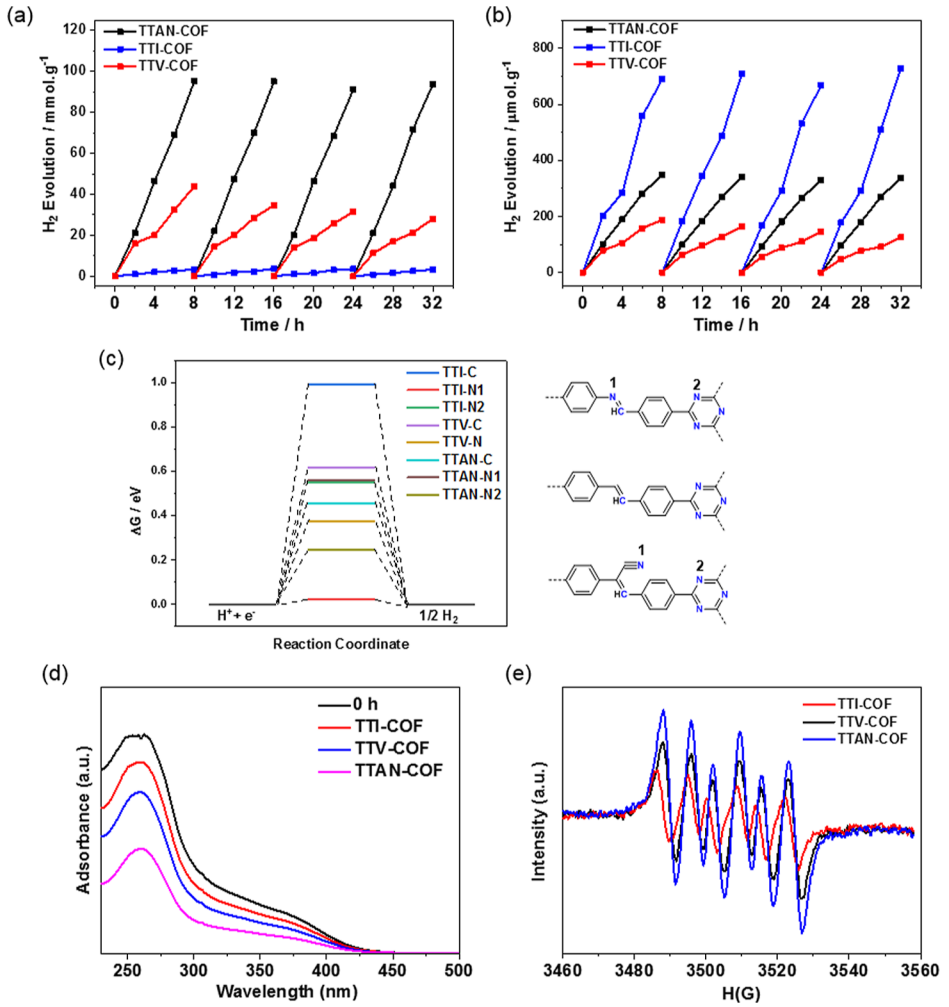

Figure 5. Photocatalytic activities of TTI/TTV/TTAN-COFs. H_2 evolution test of three COFs with the Pt co-catalyst (a) and without the co-catalyst (b) over 32 h. (c) Hydrogen-binding free energy, ΔG_{H^*}, at nitrogen and carbon sites in the case of one hydrogen atom. (d) NBT reduction experiment over 30 min by three COFs. (e) Detection of superoxide radicals by electron spin resonance (ESR) spectroscopy.

TTAN-COF is higher than most of the reported sp^2 carbon-bridged COFs and is also comparable to most of COF-based HER photocatalysts (Table S8). It should be noted that TTI-COF with the highest crystallinity BET surface area among the three COFs shows the lowest HER activity, suggesting the crucial role of sp^2 carbon bridge to enhance the HER performance of the photocatalyst. In addition, the HER activity of acrylonitrile-linked TTAN-COF was unexpectedly significantly better than that of vinylene-linked TTV-COF, which breaks the common perception. In order to exclude the positive effect of higher crystallinity and BET surface area of TTAN-COF, the photocatalytic activity of the TTAN-CMP with the lower crystallinity and porosity (BET surface area: 482.48 $m^2\ g^{-1}$) than TTV-COF was investigated (Figure S12). As expected, TTAN-CMP (3 wt % Pt as co-catalyst) still exhibited higher photocatalytic HER activities (6.00 mmol $g^{-1}\ h^{-1}$) compared to TTV-COF, confirming that the photocatalytic activity is intrinsically driven by the chemical structure of linkages in COFs while the crystallinity and surface area are the secondary factors.

The TEM images of the recovered photocatalysts clearly show the distribution of Pt nanoparticles (NPs) in three COFs (Figure S14). It can be seen that Pt NPs were uniformly distributed in TTAN-COF with the smallest average particle size in TTAN-COF, which could be attributed to the anchoring effect of cyano groups in acrylonitrile linkage to Pt NPs. There was also a certain coordination interaction between imine N in TTI-COF and Pt NPs but weaker than that of the cyano group; hence, Pt NPs were uniformly distributed in TTI-COF with a slightly larger average particle size. In contrast, significant aggregation of Pt NPs occurred on vinylene-linked TTV-COF. Although the photocatalytic HER activity is essentially determined by the structure of the material, we believe that the particle size of the Pt co-catalyst and the interaction with COFs still play a non-negligible auxiliary role. Furthermore, the weight percentage of Pt NPs loading on the recovered three COFs after 8 h of photocatalytic HER was measured. The results showed that the Pt co-catalyst loading on TTI/TTV/TTAN-COFs and TTAN-CMP photocatalysts were 2.4, 1.7, 1.6, and 1.4 wt %, respectively, implying that the actual loading of Pt NPs is directly related to the specific surface areas of COFs rather than the metal−ligand interaction. Therefore, we further determined that the good photocatalytic activity of TTAN-COF is intrinsically derived from the chemical structure of the acrylonitrile linkage, rather than the secondary factors such as surface area and Pt loading.

https://doi.org/10.1021/acscatal.2c02908
ACS Catal. 2022, 12, 10718−10726

Three pure COFs were still capable of producing H_2 with an average HER rates of 91.07, 23.38, and 43.66 μmol g^{-1} h^{-1} for TTI/TTV/TTAN-COF in the absence of Pt co-catalyst (Figure 5b), implying a higher overpotential on the active site of COFs which inhibit the process of HER. According to previous reports, the N sites, especially the imine N, in the linkage of COFs were the main active site for HER.[50,57] Therefore, DFT calculations were performed to investigate the H_2 evolution reaction pathways and the optimal HER active sites in the three COFs (Figure 5c). Specifically, the energy barrier for adsorbed H* intermediates (ΔG_{H^*}) at the imine N site (0.02 eV) was significantly lower than that at other sites, implying the high activity of imine N in HER. The highest HER activity of pure TTI-COF can also be explained. In contrast, triazine N sites were the main HER active sites in TTV/TTAN-COF. The ΔG_{H^*} at triazine N sites showed a decreasing trend in TTI/TTV/TTAN-COF, which were 0.55, 0.38, and 0.25 eV, respectively, indicating that acrylonitrile linkage effectively decreases the energy barrier at triazine N sites for H_2 formation. Overall, the linkage plays an important role in the hydrogen production efficiency of COFs. Imine linkages with low overpotentials are suitable for HER of pure COFs, while the optoelectronic properties of COFs are the main factors determining the HER activity in the presence of Pt co-catalysts.

Such high HER activities of TTI-COF and TTAN-COF remained steady during the 32 h of photocatalytic HER experiments under light irradiation (Figure 5a,b), while TTV-COF showed slight decrease of HER activity. Furthermore, the PXRD analysis of the COFs after a long-term photocatalytic reaction showed the retention of crystallinity in TTI-COF and TTAN-COF but the collapse of the crystalline structure in TTV-COF (Figure S15), which resulted in the gradual diminution of HER activity. Such results were in line with the photo-stability test, demonstrating the significant advantage of acrylonitrile linkage in photo-stability.

Photocatalytic Aerobic Oxidation Reaction. Photocatalytic aerobic oxidation is also a typical application field of COF-based photocatalysts. Oxygen molecules can be stimulated by excited COF photocatalysts under light irradiation to generate reactive oxygen species (ROS), including superoxide anion radical ($O_2^{\bullet-}$), singlet oxygen ($^1O_2$), hydroxyl radical ($^\bullet$OH), and hydrogen peroxide (H_2O_2). Notably, triazine-functionalized COFs have been reported to induce contaminant degradation and organic reactions by producing $O_2^{\bullet-}$;[30,31] therefore, production efficiency of $O_2^{\bullet-}$ via the three COFs were investigated by nitro blue tetrazolium (NBT) reduction and radical trapping experiments[58] (Figure 5d,e). NBT can be reduced by all the three COFs under visible light, and the ratio of $O_2^{\bullet-}$ generation rates by TTI/TTV/TTAN-COF was determined to be 1:1.35:3.08. The 5,5-dimethyl-1-pyrroline-*N*-oxide (DMPO) was used as the particular trapping agent for $O_2^{\bullet-}$. After the mixture with DMPO solution under light irradiation, typical signals of DMPO−OOH were detected by ESR spectroscopy for TTI/TTV/TTAN-COF with an increasing order of signal intensity. From these results, it is clear that the acrylonitrile linkage endowed TTAN-COF with the best generation rate of $O_2^{\bullet-}$ under light irradiation.

The hydroxylation reactions of boronic acids, mainly induced by $O_2^{\bullet-}$, were selected to evaluate the photocatalytic aerobic oxidation activity of three COFs. Specifically, the transformation of 4-cyanophenylboronic acid into 4-cyanophenol was chosen as the model reaction, with *N*,*N*-diisopropylethylamine (DIPEA) as the sacrificial agent under an O_2 atmosphere (Table S9). After visible irradiation for 5 h, the yield of 4-cyanophenol reached 67, 83, and 99% with TTI/TTV/TTAN-COF as the photocatalyst. This result indicated that the acrylonitrile linkage also endowed TTAN-COF with the highest photocatalytic activity in the aerobic oxidation reaction. Control experiments indicated that photocatalyst, O_2, and light were necessary to this reaction, which implied that the reactions were aerobic oxidation reactions induced by photocatalysts. The activities of the TTI/TTAN-COF were retained after five catalytic cycles with retention of crystallinity (Figure S16), while a gradual decay of the activity was observed in TTV-COF with the increase of catalytic cycle (Figure S17) and the crystalline structure was completely collapsed, which are predictable.

CONCLUSIONS

In this work, imine-, vinylene-, and acrylonitrile-linked TTI/TTV/TTAN-COFs based on functionalized N_3 structures were synthesized and the effect of linkages on the performance of COFs was also investigated in detail. It was found that the acrylonitrile linkage endowed the COFs with the best performance in all aspects among the three linkages. First, the acrylonitrile linkage provided TTAN-COF with both good chemical and photostability. In contrast, the chemical stability of TTI-COF and the photostability of TTV-COF are not good enough. Moreover, TTAN-COF with acrylonitrile linkage showed a strong fluorescence effect, photoelectric response, and higher conduction efficiency of photogenerated carriers. The PLQY of TTAN-COF in the solid state is as high as 35.37%, which is superior to all reported COFs even without introducing AIE chromophores. Further, TTAN-COF showed comprehensive and efficient photocatalytic activity in both photocatalytic HER reaction and aerobic oxidation reaction with good durability. A HER efficiency of 11.94 mmol g^{-1} h^{-1} (BET surface area: 739.28 $m^2 \cdot g^{-1}$) reached a high level among COF photocatalytic materials (in the presence of the Pt co-catalyst). This work demonstrates the critical role of acrylonitrile linkage in the enhancement of photoluminescence and photocatalytic performance of COFs, especially compared to vinylene linkage. It is expected to develop acrylonitrile linked COF-based high-performance fluorescent and photocatalyst materials by a further functionalized monomer design and derivatization of cyano substituents.

ASSOCIATED CONTENT

Supporting Information

The Supporting Information is available free of charge at https://pubs.acs.org/doi/10.1021/acscatal.2c02908.

General information, method, synthetic procedure, structure simulations, characterization results (including N_2 adsorption experiment, SEM images, DRS spectra, CV curves, and Mott−Schottky plots), DFT calculation results, and procedure and results supplementing photocatalytic experiments (PDF)

AUTHOR INFORMATION

Corresponding Author

Yaqi Cai − *State Key Laboratory of Environmental Chemistry and Ecotoxicology, Research Center for Eco-Environmental Sciences, Chinese Academy of Sciences, Beijing 100085, P. R.China; University of Chinese Academy of Sciences, Beijing*

https://doi.org/10.1021/acscatal.2c02908
ACS Catal. 2022, 12, 10718−10726

100049, P. R. China; School of Environment, Hangzhou Institute for Advanced Study, University of Chinese Academy of Sciences, Hangzhou 310024, P. R. China; orcid.org/0000-0002-2805-5535; Email: caiyaqi@rcees.ac.cn

Authors

Yongliang Yang − *State Key Laboratory of Environmental Chemistry and Ecotoxicology, Research Center for Eco-Environmental Sciences, Chinese Academy of Sciences, Beijing 100085, P. R.China; University of Chinese Academy of Sciences, Beijing 100049, P. R. China*

Na Luo − *State Key Laboratory of Environmental Chemistry and Ecotoxicology, Research Center for Eco-Environmental Sciences, Chinese Academy of Sciences, Beijing 100085, P. R.China; University of Chinese Academy of Sciences, Beijing 100049, P. R. China*

Shiyun Lin − *MOE Key Laboratory of Organic OptoElectronics and Molecular Engineering, Department of Chemistry, Tsinghua University, Beijing 100084, P. R. China;* orcid.org/0000-0002-9394-2149

Huan Yao − *Division of Chemistry and Analytical Science, National Institute of Metrology, Beijing 100029, P. R. China*

Complete contact information is available at: https://pubs.acs.org/10.1021/acscatal.2c02908

Notes

The authors declare no competing financial interest.

■ ACKNOWLEDGMENTS

This work was jointly supported by the National Natural Science Foundation of China (22036007) and the National Key R&D Program of China (2019YFC1804501).

■ REFERENCES

(1) Côté, A. P.; Benin, A. I.; Ockwig, N. W.; O'Keeffe, M.; Matzger, A. J.; Yaghi, O. M. Porous, crystalline, covalent organic frameworks. *Science* **2005**, *310*, 1166−1170.

(2) Kandambeth, S.; Biswal, B. P.; Chaudhari, H. D.; Rout, K. C.; Kunjattu H, H. S.; Mitra, S.; Karak, S.; Das, A.; Mukherjee, R.; Kharul, U. K.; Banerjee, R. Selective Molecular Sieving in Self-Standing Porous Covalent-Organic-Framework Membranes. *Adv. Mater.* **2017**, *29*, 1603945.

(3) Yang, C. X.; Liu, C.; Cao, Y. M.; Yan, X. P. Facile room-temperature solution-phase synthesis of a spherical covalent organic framework for high-resolution chromatographic separation. *Chem. Commun.* **2015**, *51*, 12254−12257.

(4) Ding, S. Y.; Dong, M.; Wang, Y. W.; Chen, Y. T.; Wang, H. Z.; Su, C. Y.; Wang, W. Thioether-Based Fluorescent Covalent Organic Framework for Selective Detection and Facile Removal of Mercury(II). *J. Am. Chem. Soc.* **2016**, *138*, 3031−3037.

(5) Bagheri, A. R.; Aramesh, N.; Haddad, P. R. Applications of covalent organic frameworks and their composites in the extraction of pesticides from different samples. *J. Chromatogr. A* **2022**, *1661*, 462612.

(6) Li, H.; Pan, Q.; Ma, Y.; Guan, X.; Xue, M.; Fang, Q.; Yan, Y.; Valtchev, V.; Qiu, S. Three-Dimensional Covalent Organic Frameworks with Dual Linkages for Bifunctional Cascade Catalysis. *J. Am. Chem. Soc.* **2016**, *138*, 14783−14788.

(7) Fang, Q. R.; Gu, S.; Zheng, J.; Zhuang, Z. B.; Qiu, S. L.; Yan, Y. S. 3D Microporous Base-Functionalized Covalent Organic Frameworks for Size-Selective Catalysis. *Angew. Chem., Int. Ed.* **2014**, *53*, 2878−2882.

(8) Shinde, D. B.; Kandambeth, S.; Pachfule, P.; Kumar, R. R.; Banerjee, R. Bifunctional covalent organic frameworks with two dimensional organocatalytic micropores. *Chem. Commun.* **2015**, *51*, 310−313.

(9) Huang, S.; Chen, K.; Li, T.-T. Porphyrin and phthalocyanine based covalent organic frameworks for electrocatalysis. *Coord. Chem. Rev.* **2022**, *464*, 214563.

(10) Xu, H.; Tao, S.; Jiang, D. Proton conduction in crystalline and porous covalent organic frameworks. *Nat. Mater.* **2016**, *15*, 722−726.

(11) DeBlase, C. R.; Silberstein, K. E.; Truong, T. T.; Abruña, H. D.; Dichtel, W. R. β-Ketoenamine-Linked Covalent Organic Frameworks Capable of Pseudocapacitive Energy Storage. *J. Am. Chem. Soc.* **2013**, *135*, 16821−16824.

(12) Chandra, S.; Kundu, T.; Dey, K.; Addicoat, M.; Heine, T.; Banerjee, R. Interplaying Intrinsic and Extrinsic Proton Conductivities in Covalent Organic Frameworks. *Chem. Mater.* **2016**, *28*, 1489−1494.

(13) Chen, X.; Sun, W.; Wang, Y. Covalent Organic Frameworks for Next-Generation Batteries. *Chemelectrochem* **2020**, *7*, 3905−3926.

(14) Calik, M.; Auras, F.; Salonen, L. M.; Bader, K.; Grill, I.; Handloser, M.; Medina, D. D.; Dogru, M.; Löbermann, F.; Trauner, D.; Hartschuh, A.; Bein, T. Extraction of photogenerated electrons and holes from a covalent organic framework integrated heterojunction. *J. Am. Chem. Soc.* **2014**, *136*, 17802−17807.

(15) Dogru, M.; Handloser, M.; Auras, F.; Kunz, T.; Medina, D.; Hartschuh, A.; Knochel, P.; Bein, T. A Photoconductive Thienothiophene-Based Covalent Organic Framework Showing Charge Transfer Towards Included Fullerene. *Angew. Chem., Int. Ed.* **2013**, *52*, 2920−2924.

(16) Bessinger, D.; Ascherl, L.; Auras, F.; Bein, T. Spectrally Switchable Photodetection with Near-Infrared-Absorbing Covalent Organic Frameworks. *J. Am. Chem. Soc.* **2017**, *139*, 12035−12042.

(17) Yildirim, O.; Bonomo, M.; Barbero, N.; Atzori, C.; Civalleri, B.; Bonino, F.; Viscardi, G.; Barolo, C. Application of metal-organic frameworks and covalent organic frameworks as (photo) active material in hybrid photovoltaic technologies. *Energies* **2020**, *13*, 5602.

(18) Li, S.; Zou, J.; Tan, L.; Huang, Z.; Liang, P.; Meng, X. Covalent organic frameworks: from linkages to biomedical applications. *Chem. Eng. J.* **2022**, *446*, 137148.

(19) Wang, L.; Hong, S.; Yang, Y.; Song, Y.; Wang, L. Covalent Organic Frameworks for Electrochemical Sensors: Recent Research and Future Prospects. *Curr. Anal. Chem.* **2022**, *18*, 646−663.

(20) Qian, H.-L.; Wang, Y.; Yan, X.-P. Covalent organic frameworks for environmental analysis. *Trac. Trends Anal. Chem.* **2022**, *147*, 116516.

(21) Feng, X.; Ding, X.; Jiang, D. Covalent organic frameworks. *Chem. Soc. Rev.* **2012**, *41*, 6010−6022.

(22) Lohse, M. S.; Bein, T. Covalent Organic Frameworks: Structures, Synthesis, and Applications. *Adv. Funct. Mater.* **2018**, *28*, 1705553.

(23) Zhao, J.; Ren, J.; Zhang, G.; Zhao, Z.; Liu, S.; Zhang, W.; Chen, L. Donor-Acceptor Type Covalent Organic Frameworks. *Chem.—Eur J.* **2021**, *27*, 10781−10797.

(24) Wang, H.; Wang, H.; Wang, Z.; Tang, L.; Zeng, G.; Xu, P.; Chen, M.; Xiong, T.; Zhou, C.; Li, X.; Huang, D.; Zhu, Y.; Wang, Z.; Tang, J. Covalent organic framework photocatalysts: structures and applications. *Chem. Soc. Rev.* **2020**, *49*, 4135−4165.

(25) Banerjee, T.; Gottschling, K.; Savasci, G.; Ochsenfeld, C.; Lotsch, B. V. H2 Evolution with Covalent Organic Framework Photocatalysts. *ACS Energy Lett.* **2018**, *3*, 400−409.

(26) Stegbauer, L.; Schwinghammer, K.; Lotsch, B. V. A hydrazone-based covalent organic framework for photocatalytic hydrogen production. *Chem. Sci.* **2014**, *5*, 2789−2793.

(27) Wei, P. F.; Qi, M. Z.; Wang, Z. P.; Ding, S. Y.; Yu, W.; Liu, Q.; Wang, L. K.; Wang, H. Z.; An, W. K.; Wang, W. Benzoxazole-Linked Ultrastable Covalent Organic Frameworks for Photocatalysis. *J. Am. Chem. Soc.* **2018**, *140*, 4623−4631.

(28) Li, Z. P.; Zhi, Y. F.; Shao, P. P.; Xia, H.; Li, G. S.; Feng, X.; Chen, X.; Shi, Z.; Liu, X. M. Covalent organic framework as an efficient, metal-free, heterogeneous photocatalyst for organic transformations under visible light. *Appl. Catal., B* **2019**, *245*, 334−342.

(29) Chen, R.; Shi, J. L.; Ma, Y.; Lin, G.; Lang, X.; Wang, C. Designed Synthesis of a 2D Porphyrin-Based sp2 Carbon-Conjugated Covalent Organic Framework for Heterogeneous Photocatalysis. *Angew. Chem., Int. Ed.* **2019**, *58*, 6430−6434.
(30) He, S. J.; Yin, B.; Niu, H. Y.; Cai, Y. Q. Targeted synthesis of visible-light-driven covalent organic framework photocatalyst via molecular design and precise construction. *Appl. Catal., B* **2018**, *239*, 147−153.
(31) Yang, Y. L.; Niu, H. Y.; Xu, L.; Zhang, H.; Cai, Y. Q. Triazine functionalized fully conjugated covalent organic framework for efficient photocatalysis. *Appl. Catal., B* **2020**, *269*, 118799.
(32) Pachfule, P.; Acharjya, A.; Roeser, J.; Langenhahn, T.; Schwarze, M.; Schomäcker, R.; Thomas, A.; Schmidt, J. Diacetylene Functionalized Covalent Organic Framework (COF) for Photocatalytic Hydrogen Generation. *J. Am. Chem. Soc.* **2018**, *140*, 1423−1427.
(33) Vyas, V. S.; Haase, F.; Stegbauer, L.; Savasci, G.; Podjaski, F.; Ochsenfeld, C.; Lotsch, B. V. A tunable azine covalent organic framework platform for visible light-induced hydrogen generation. *Nat. Commun.* **2015**, *6*, 8508.
(34) Chen, R.; Wang, Y.; Ma, Y.; Mal, A.; Gao, X.-Y.; Gao, L.; Qiao, L.; Li, X.-B.; Wu, L.-Z.; Wang, C. Rational design of isostructural 2D porphyrin-based covalent organic frameworks for tunable photocatalytic hydrogen evolution. *Nat. Commun.* **2021**, *12*, 1354.
(35) Lu, M.; Liu, J.; Li, Q.; Zhang, M.; Liu, M.; Wang, J. L.; Yuan, D. Q.; Lan, Y. Q. Rational Design of Crystalline Covalent Organic Frameworks for Efficient CO2 Photoreduction with H_2O. *Angew. Chem., Int. Ed.* **2019**, *58*, 12392−12397.
(36) Yang, S.; Hu, W.; Zhang, X.; He, P.; Pattengale, B.; Liu, C.; Cendejas, M.; Hermans, I.; Zhang, X.; Zhang, J.; Huang, J. 2D Covalent Organic Frameworks as Intrinsic Photocatalysts for Visible Light-Driven CO2 Reduction. *J. Am. Chem. Soc.* **2018**, *140*, 14614−14618.
(37) Bi, S.; Meng, F.; Zhang, Z.; Wu, D.; Zhang, F. Covalent Organic Frameworks with trans-Dimensionally Vinylene-linked π-Conjugated Motifs. *Chem. Res. Chin. Univ.* **2022**, *38*, 382−395.
(38) Bi, S.; Yang, C.; Zhang, W.; Xu, J.; Liu, L.; Wu, D.; Wang, X.; Han, Y.; Liang, Q.; Zhang, F. Two-dimensional semiconducting covalent organic frameworks via condensation at arylmethyl carbon atoms. *Nat. Commun.* **2019**, *10*, 2467.
(39) Lyu, H.; Diercks, C. S.; Zhu, C.; Yaghi, O. M. Porous Crystalline Olefin-Linked Covalent Organic Frameworks. *J. Am. Chem. Soc.* **2019**, *141*, 6848−6852.
(40) Bi, S.; Thiruvengadam, P.; Wei, S.; Zhang, W.; Zhang, F.; Gao, L.; Xu, J.; Wu, D.; Chen, J. S.; Zhang, F. Vinylene-Bridged Two-Dimensional Covalent Organic Frameworks via Knoevenagel Condensation of Tricyanomesitylene. *J. Am. Chem. Soc.* **2020**, *142*, 11893−11900.
(41) Meng, F.; Bi, S.; Sun, Z.; Jiang, B.; Wu, D.; Chen, J. S.; Zhang, F. Synthesis of Ionic Vinylene-Linked Covalent Organic Frameworks through Quaternization-Activated Knoevenagel Condensation. *Angew. Chem., Int. Ed.* **2021**, *60*, 13614−13620.
(42) Bi, S.; Zhang, Z.; Meng, F.; Wu, D.; Chen, J.-S.; Zhang, F. Heteroatom-Embedded Approach to Vinylene-Linked Covalent Organic Frameworks with Isoelectronic Structures for Photoredox Catalysis. *Angew. Chem., Int. Ed.* **2022**, *61*, No. e202111627.
(43) Wang, Z.; Yang, Y.; Zhao, Z.; Zhang, P.; Zhang, Y.; Liu, J.; Ma, S.; Cheng, P.; Chen, Y.; Zhang, Z. Green synthesis of olefin-linked covalent organic frameworks for hydrogen fuel cell applications. *Nat. Commun.* **2021**, *12*, 1982.
(44) Pastoetter, D. L.; Xu, S.; Borrelli, M.; Addicoat, M.; Biswal, B. P.; Paasch, S.; Dianat, A.; Thomas, H.; Berger, R.; Reineke, S.; Brunner, E.; Cuniberti, G.; Richter, M.; Feng, X. Synthesis of Vinylene-Linked Two-Dimensional Conjugated Polymers via the Horner-Wadsworth-Emmons Reaction. *Angew. Chem., Int. Ed.* **2020**, *59*, 23620−23625.
(45) Halder, A.; Kandambeth, S.; Biswal, B. P.; Kaur, G.; Roy, N. C.; Addicoat, M.; Salunke, J. K.; Banerjee, S.; Vanka, K.; Heine, T.; Verma, S.; Banerjee, R. Decoding the Morphological Diversity in Two Dimensional Crystalline Porous Polymers by Core Planarity Modulation. *Angew. Chem., Int. Ed.* **2016**, *55*, 7806−7810.
(46) Xu, S.; Liao, Z.; Dianat, A.; Park, S.-W.; Addicoat, M. A.; Fu, Y.; Pastoetter, D. L.; Fabozzi, F. G.; Liu, Y.; Cuniberti, G.; Richter, M.; Hecht, S.; Feng, X. Combination of Knoevenagel Polycondensation and Water-Assisted Dynamic Michael-Addition-Elimination for the Synthesis of Vinylene-Linked 2D Covalent Organic Frameworks. *Angew. Chem., Int. Ed.* **2022**, *61*, No. e202202492.
(47) Jin, E.; Li, J.; Geng, K.; Jiang, Q.; Xu, H.; Xu, Q.; Jiang, D. Designed synthesis of stable light-emitting two-dimensional sp(2) carbon-conjugated covalent organic frameworks. *Nat. Commun.* **2018**, *9*, 4143.
(48) Acharjya, A.; Pachfule, P.; Roeser, J.; Schmitt, F. J.; Thomas, A. Vinylene-Linked Covalent Organic Frameworks by Base-Catalyzed Aldol Condensation. *Angew. Chem., Int. Ed.* **2019**, *58*, 14865−14870.
(49) Jadhav, T.; Fang, Y.; Liu, C. H.; Dadvand, A.; Hamzehpoor, E.; Patterson, W.; Jonderian, A.; Stein, R. S.; Perepichka, D. F. Transformation between 2D and 3D Covalent Organic Frameworks via Reversible [2 + 2] Cycloaddition. *J. Am. Chem. Soc.* **2020**, *142*, 8862−8870.
(50) Zhao, Z.; Zheng, Y.; Wang, C.; Zhang, S.; Song, J.; Li, Y.; Ma, S.; Cheng, P.; Zhang, Z.; Chen, Y. Fabrication of Robust Covalent Organic Frameworks for Enhanced Visible-Light-Driven H2 Evolution. *ACS Catal.* **2021**, *11*, 2098−2107.
(51) Mei, J.; Leung, N. L.; Kwok, R. T.; Lam, J. W.; Tang, B. Z. Aggregation-Induced Emission: Together We Shine, United We Soar! *Chem. Rev.* **2015**, *115*, 11718−11940.
(52) Li, Y.; Li, F.; Zhang, H.; Xie, Z.; Xie, W.; Xu, H.; Li, B.; Shen, F.; Ye, L.; Hanif, M.; Ma, D.; Ma, Y. Tight intermolecular packing through supramolecular interactions in crystals of cyano substituted oligo(para-phenylene vinylene): a key factor for aggregation-induced emission. *Chem. Commun.* **2007**, *3*, 231−233.
(53) An, B. K.; Kwon, S. K.; Jung, S. D.; Park, S. Y. Enhanced emission and its switching in fluorescent organic nanoparticles. *J. Am. Chem. Soc.* **2002**, *124*, 14410−14415.
(54) Gao, Q.; Li, X.; Ning, G. H.; Leng, K.; Tian, B.; Liu, C.; Tang, W.; Xu, H. S.; Loh, K. P. Highly photoluminescent two-dimensional imine-based covalent organic frameworks for chemical sensing. *Chem. Commun.* **2018**, *54*, 2349−2352.
(55) Yin, H.; Chen, J.; Guan, P.; Zheng, D.; Kong, Q.; Yang, S.; Zhou, P.; Yang, B.; Pullerits, T.; Han, K. Controlling Photoluminescence and Photocatalysis Activities in Lead-Free Cs2 Ptx Sn1-x Cl6 Perovskites via Ion Substitution. *Angew. Chem., Int. Ed.* **2021**, *60*, 22693−22699.
(56) Yang, J.; Acharjya, A.; Ye, M. Y.; Rabeah, J.; Li, S.; Kochovski, Z.; Youk, S.; Roeser, J.; Grüneberg, J.; Penschke, C.; Schwarze, M.; Wang, T.; Lu, Y.; Krol, R.; Oschatz, M.; Schomäcker, R.; Saalfrank, P.; Thomas, A. Protonated Imine-Linked Covalent Organic Frameworks for Photocatalytic Hydrogen Evolution. *Angew. Chem., Int. Ed.* **2021**, *60*, 19797−19803.
(57) Wan, Y.; Wang, L.; Xu, H.; Wu, X.; Yang, J. A Simple Molecular Design Strategy for Two-Dimensional Covalent Organic Framework Capable of Visible-Light-Driven Water Splitting. *J. Am. Chem. Soc.* **2020**, *142*, 4508−4516.
(58) Nosaka, Y.; Nosaka, A. Y. Generation and Detection of Reactive Oxygen Species in Photocatalysis. *Chem. Rev.* **2017**, *117*, 11302−11336.

https://doi.org/10.1021/acscatal.2c02908
ACS Catal. 2022, 12, 10718−10726